Journal of Energy Storage 144 (2026) 119691

Contents lists available at ScienceDirect

Journal of Energy Storage

journal homepage: www.elsevier.com/locate/est

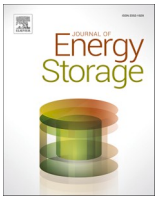

Research papers

Extended operating range of PCM steam generators

Larissa Dietz, Michael Fiss, Wolf-Dieter Steinmann, Inga Bürger, Andrea Gutierrez *

Institute of Engineering Thermodynamics, German Aerospace Center (DLR), Pfaffenwaldring 38 – 40, 70569, Stuttgart, Germany

ARTICLE INFO

Keywords:
Phase change material storage
Steam generator
Fluid control strategies
Experimental setup
Model validation

ABSTRACT

For steam-driven industrial processes, Latent Heat-Thermal Energy Storages are a promising option to increase their flexibility regarding fluctuating renewable energies. This work provides the foundation for the quantitative analysis of control strategies for such phase change material steam generators and their practical system integration in once-through operation. Experiments are conducted in a self-built, one-kilowatt-scale single-tube test rig with extensive measurement equipment and precise fluid control, employing water/steam as the heat transfer fluid and PLUSICE A133 as the phase change material. Tests at different mass flow rates and pressures of the HTF show the strong correlation between the mass flow rate of the HTF and the storage power in practice. In addition, it is found that a reduction in the mass flow rate significantly increases the effective capacity during charging and discharging: By halving the mass flow rate during charging, it can be increased from 62 % to 77 % at a pressure level of 6.7 bar and from 3 % to 21 % at a pressure level of 3.0 bar. An increased pressure level can further increase the usable capacity of the storage material. The experimental results thus prove the effectiveness and relevance of considering heat transfer fluid control aspects already in the storage design process.

Furthermore, the validation of a numerical storage design model shows that the peak power during charging can be accurately predicted by the model with deviations <3 %. With sufficiently long charging processes, also the simulated transient power profiles and outlet temperatures of the heat transfer fluid can be used reliably for storage design.

1. Introduction

Thermal energy storage systems are crucial to improve the efficiency of the energy use, for the electrification of industrial processes and for power generation, increasing shares of energy supplied based on fluctuating renewable sources [1].

Especially for steam-driven industrial processes up to 300 °C and for the integration of heat pumps [2] as well as for power generation [3], Latent Heat-Thermal Energy Storage (LH-TES) is a promising technology [4]. The storage materials in LH-TES, so called phase change materials (PCM), provide a high energy density within a narrow temperature range as the dominant share of the energy is stored as latent heat. The simultaneous and almost isothermal phase change processes in the PCM and the HTF enable charging and discharging with small temperature differences between the PCM and the steam, resulting in high charging and discharging efficiencies.

In the context of steam applications, LH-TES systems hold strong potential to significantly enhance energy efficiency and operational flexibility, especially in the food industry, the paper industry and some processes of the chemical industry [2]. These sectors typically demand process steam in a temperature range between 100 °C and 250 °C [2], aligning well with the capabilities of LH-TES. Table 1 presents examples of steam use and the corresponding temperature ranges in various industry sectors in Germany.

Typical candidate PCMs, such as inorganic salts, are characterised by low thermal conductivities, so the first key challenge is the identification of cost-effective heat exchanger concepts with a high degree of PCM utilisation and a needs-based power-to-capacity ratio during charging and discharging. Most common for LH-TES is the shell-and-tube design with the storage material in the shell and the heat transfer fluid (HTF) flowing in the tubes. The heat transfer in the device is enhanced by extended heat transfer surfaces, through additives that increase the effective thermal conductivity of the PCM or through a combination of both [5]. Due to the changes in phase distribution in the storage volume, resulting in variations of the heat transfer resistance, the transmitted power is transient for constant inlet conditions of the working medium. Theologou et al. [6] comprehensively summarise the current literature on realised finned LH-TES of this type.

* Corresponding author.
E-mail address: Andrea.GutierrezRojas@dlr.de (A. Gutierrez).

https://doi.org/10.1016/j.est.2025.119691
Received 13 April 2025; Received in revised form 29 October 2025; Accepted 30 November 2025
Available online 5 December 2025

Nomenclature

Formula symbols

f	liquid fraction
c_p	specific heat capacity (J/(kg K))
g	gravitational acceleration (m/s^2)
$\dot{H}$	enthalpy flow (W)
L	level (m)
$\dot{m}$	mass flow rate (kg/s)
m	mass (kg)
p	pressure (Pa)
Q	stored heat (J)
$\dot{Q}$	thermal power (W)
t	time (s)
T	temperature (K)
Δ	difference
Δh	phase change enthalpy (J/kg)
ρ	density (kg/m^3)
x	steam content (−)

Abbreviations

DHTS	dominant heat transfer surface
DSC	differential scanning calorimetry
HTF	heat transfer fluid
LH-TES	Latent Heat-Thermal Energy Storage
PC	phase change
PCM	phase change material

Subscripts

b	bottom
end	end of experiment
char	charging
dis	discharging
HTF	heat transfer fluid
i	time step
in	inlet
liq	liquidus
out	outlet
PCM	phase change material
sat	saturation
sl	solid/liquid
sol	solidus
stor	storage
start	start of experiment
top	top

1.1. Operating modes for LH-TES

An important additional critical aspect to consider in the development of PCM storage systems is the specification of fluid control strategies to operate the storage system according to the boundary conditions of a specific application while maximising the exploitation of the storage material. Various operating modes can be combined with suitable control strategies. The operating mode is defined by the permanently installed infrastructure for the integration of the LH-TES into the respective system, the control strategy by the conditions of the working fluid.

The most straight-forward operating mode, besides the more complex recirculation mode (Fig. 1, left and centre), is once-through operation (Fig. 1, right). Here, the complete inlet mass flow rate fed to the storage is transferred to the connected steam consumer.

1.2. Control strategies for Latent Heat-Thermal Energy Storage systems

To utilise the once-through mode in real applications, reliable control strategies that consider the transient characteristics of LH-TES depending on the state of charge are of crucial importance. Options for control strategies of the HTF are the control of the pressure, of the mass flow rate or both during the charging/discharging process.

Pressure control in LH-TES for steam generation in finned shell-and-tube design has been discussed extensively in the scientific literature and both constant pressure operation and sliding pressure operation are common control strategies. In constant pressure operation, the steam pressure and temperature remain constant, while the power transferred between the storage and the HTF (storage power) – and thus the mass flow rate of steam that can be generated – decreases. In sliding pressure operation on the other hand, the storage power is more stable, but pressure and temperature of the steam therefore decrease.

Garcia et al. [7] show the results for a 300-kWh LH-TES with sodium nitrate in sliding pressure for discharging. Laing et al. [8,9] extend the operating range and test a 700-kWh PCM storage module with sodium nitrate at constant as well as at sliding pressure. The results allow a comparison between constant and sliding pressure operation, albeit on a large multi-tube system with limited measurement equipment and thus, with restricted possibilities for interpreting the interaction between the PCM and the HTF. Garcia et al. [10] additionally monitor the liquid level in the evaporator tubes during discharging and find it to have a significant influence on the storage power and the steam properties. The same team compares two identical experiments with varied mass flow rate during discharging [11]. These publications are based on more extensive measurement equipment, go into more detail on the HTF behaviour and emphasise the relation between the storage behaviour on the one hand and the pressure and mass flow rate of the HTF on the other. However, they compare different operating modes by way of example and do not systematically analyse the effects of parameter variations. Johnson et al. [12] report on a large-scale 1900-kW module [13] with sodium nitrate, integrated for the first time in a cogeneration plant, at constant pressure. Due to the applied nature of the study, the boundary conditions depend on the customer's needs and thus vary. The most recent work is the characterisation of a 200-kWh storage module with a eutectic mixture of

Table 1
Examples for steam use in industrial processes in Germany and corresponding temperature ranges [2].

Example	T (°C)	Paper	Chemicals	Sugar	Milk products	Meat	Beer	Starch
Evaporation	40–170	x	x	x	x			x
Reduction	60–140		x	x	x			x
Boiling/Simmering	70–180					x	x	
Pasteurisation	60–150				x			
Sterilisation	100–140		x		x			
Drying	40–250	x	x	x	x			x
Fractionation/Distillation	100–300		x					
Cracking	180–200		x					

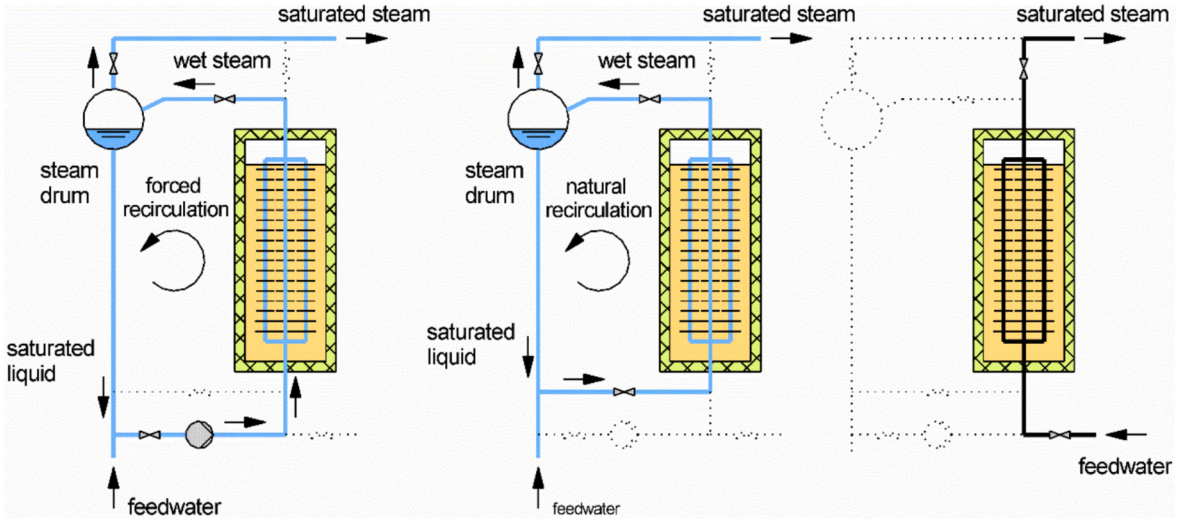

Fig. 1. Available operating modes for discharging: Forced recirculation (left), natural recirculation (centre), once-through operation (right) [4].

lithium nitrate and potassium nitrate by Theologou et al. [6]. It shows parameter studies of mass flow rate and pressure with a refrigerant during discharging. The study is systematic and comprehensive, but the physical interpretation of the results is complicated by the multi-tube nature of the setup. In contrast to pressure control, less attention has been paid to controlling the mass flow rate of the HTF. However, Garcia et al. [10] suggest increasing the mass flow rate during charging at fixed pressure once natural convection in the PCM sets in and improves heat transfer in the storage.

1.3. Aims and scope

The literature analysed in the previous section either lacks sufficiently systematic and comprehensive studies for the comparison of different operating strategies or does not provide enough information for the interpretation of the observations due to limited measuring equipment and the multi-tube nature of the test setups. In addition, none of the studies analyses the fundamental practical significance of the respective operating strategies and their influence on the material efficiency of LH-TES. There is a lack of systematic and comprehensive experimental analyses with precise control of the HTF parameters and detailed monitoring of the storage during the transient charging and discharging processes for the quantitative analysis of control strategies; also, the degree of utilisation of the storage material has not yet been considered in any of the studies in detail.

The present article, together with two previous publications by Dietz et al. [14,15], aims to provide a basis for this. Experimental pressure and mass flow rate variations at a single-tube steam generator with extensive measurement equipment and advanced flow control options are presented. The goal is to optimise power control and efficient PCM utilisation. In addition, the experimental data is used for the validation of a numerical storage model. This publication thus contributes to a basis for practical system integration of once-through PCM storage.

2. Material and methods

2.1. Test section with phase change material and steam cycle

The results of this article were obtained using a test section, which is described in detail in Dietz et al. [15]. It consists of a steel tube with

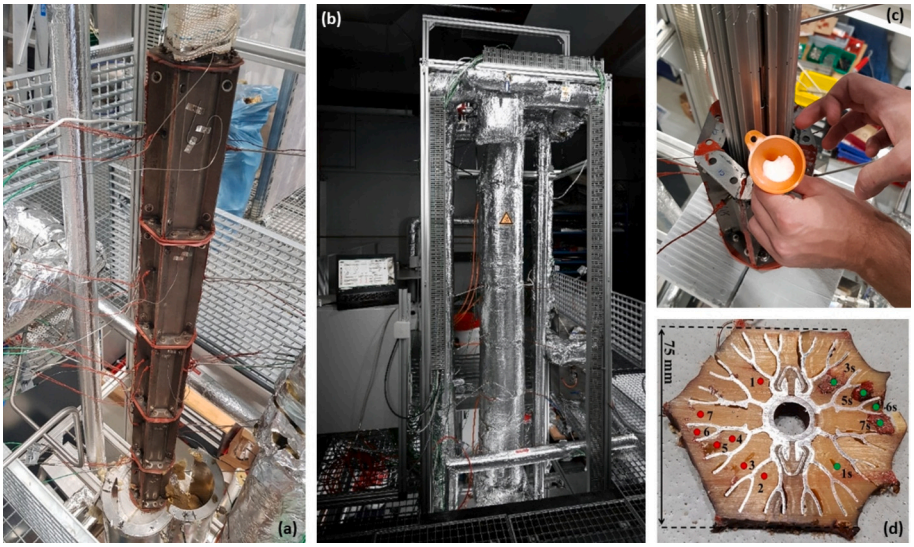

Fig. 2. Modular container (a), insulated test section (b), solid PCM during filling (c), solid PCM after cycling (d) with thermocouple positions on all levels (red) and additional thermocouple positions on level 3 (green). (For interpretation of the references to colour in this figure legend, the reader is referred to the web version of this article.)

aluminium fins, embedded in a steel container filled with the storage material. The container (Fig. 2 (a)) is 2 m high and 52 thermocouples integrated on five measuring levels distanced by 0.3 m enable temperature measurements in the PCM, in the HTF flow, at the fins and at the outer tube wall. The positions of the temperature probes in the PCM are indicated in Fig. 2 (d). Positions marked in red are implemented at all levels, positions marked in green only at level 3. Further storage specifications are summarised in Table 2.

The fluid cycle depicted in Fig. 3 charges the LH-TES element with superheated steam from the top and discharges it with subcooled water from the bottom. In the simplified schematic, the charging cycle is marked with red arrows and the discharging cycle with blue arrows. Due to the small system size, it can simultaneously and precisely control the mass flow rate and the pressure of the HTF in the system. The mass flow rate, the top and bottom pressures and temperatures of the HTF as well as the mass flow rate and inlet and outlet temperatures of the cooling water flowing through the condenser are recorded. Operation was performed in a pressure range of 1.4 bar to 6.7 bar, a temperature range of 20 °C to 200 °C and a mass flow rate range of 1.26 kg/h to 4.30 kg/h.

2.2. Processing of experimental data and metrics

2.2.1. Calculating the storage power

The storage power $\dot{Q}_{HTF}$ during charging and discharging is calculated by Eq. (1) from the enthalpy flows $\dot{H}_{HTF,in}$ and $\dot{H}_{HTF,out}$ based on pressure (p_{HTF}), temperature (T_{HTF}) and mass flow rate ($\dot{m}_{HTF}$) measurements in the HTF flow using specific enthalpies. The corresponding uncertainty areas in Figs. 7–9 are estimated based on error propagation.

$$\dot{Q}_{HTF} = \dot{H}_{HTF,out} - \dot{H}_{HTF,in} = \dot{m}_{HTF}\, h(p_{HTF}, T_{HTF})_{out} - \dot{m}_{HTF}\, h(p_{HTF}, T_{HTF})_{in} \tag{1}$$

Additionally, the storage power $\dot{Q}_{stor}$ can be approximated by Eq. (2) based on the temperature measurements in the PCM storage and its mass m_{stor}, specific heat capacity $c_{p,stor}$ and phase change enthalpy $\Delta h_{PCM,sl}$ as well as the liquid fraction f.

$$\dot{Q}_{stor} \approx \frac{\Delta Q_{stor}}{\Delta t} = \frac{Q_{stor,i} - Q_{stor,i-1}}{\Delta t} = \frac{\left(m_{stor}\, c_{p,stor}\, T_{stor} + f \Delta h_{PCM,sl}\right)_i - \left(m_{stor}\, c_{p,stor}\, T_{stor} + f \Delta h_{PCM,sl}\right)_{i-1}}{\Delta t} \tag{2}$$

Fig. 4 shows the relevant energy flow rates for the calculation of the storage power, the division of the storage into the subsection S12 to S45 and the system boundaries for the complete storage between the levels L1 and L5 during charging and between the levels L0 and L5 during discharging. The latter vary during charging and discharging due to technical limitations as discussed in Dietz et al. [15].

Table 2
Summary of storage specifications.

Specification	Value	Unit
Inner tube diameter	12.6	mm
Outer tube diameter	17.2	mm
Inner container diameter	75	mm
Finned tube length	1.2	m
Tube material	S355	–
Fin material	Aluminium	–
Attachment fin/tube	Clamped	–
PCM	PLUSICE A133 (PCM Products Ltd)	–
Nominal melting temperature PCM	133	°C
Phase change enthalpy PCM[a]	180	kJ/kg
PCM mass	4.5	kg
Latent storage capacity	225	Wh
Ratio fin mass/PCM mass	0.1795	–
Heat transfer fluid	Water/steam	–
Insulation	Electrical tracked trace heating, 5 cm of mineral wool (Fig. 2 (b))	–
Temperature sensors	Thermocouples type K (±1.6 K)	–

[a] The arithmetic mean of three internal second-cycle DSC measurements; for detailed discussion of melting and solidification behaviour refer to Dietz et al. [15].

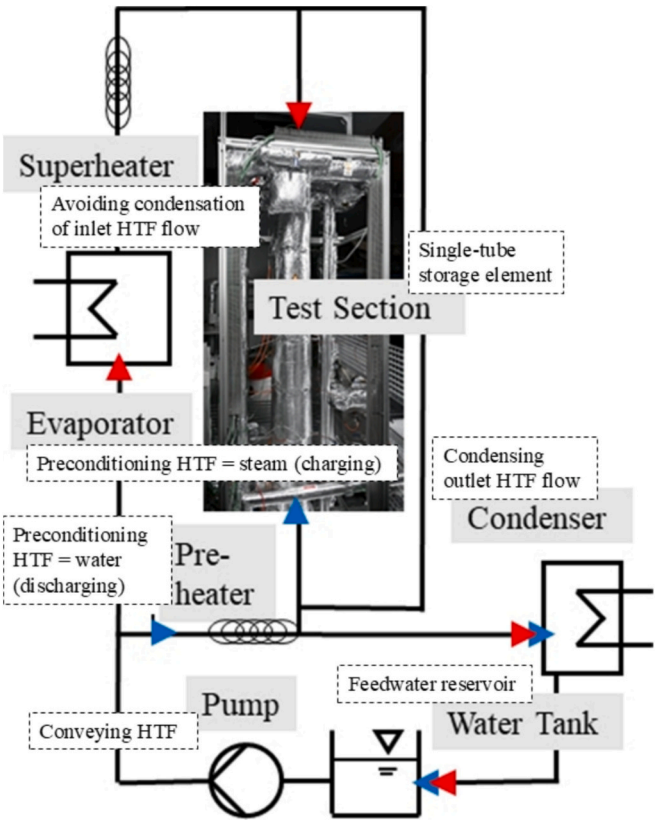

Fig. 3. Simplified schematic of steam cycle for charging and discharging of the storage element.

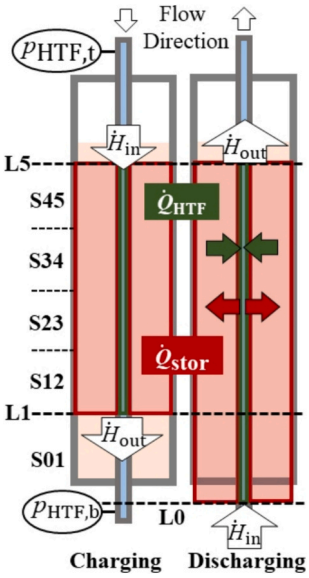

Fig. 4. System boundaries of the HTF (green) and the storage (red) and energy flow rates for the calculation of the storage power during charging and discharging. (For interpretation of the references to colour in this figure legend, the reader is referred to the web version of this article.)

2.2.2. Estimating the liquid level of the HTF

For the estimation of the liquid level L of the HTF in the pressure tubes, the pressures at the top p_{top} and the bottom p_b of the storage (Fig. 4) are used:

$$L = \frac{\left(p_{HTF,b} - p_{HTF,top}\right)}{\rho_{HTF} g}. \quad (3)$$

The variables ρ_{HTF} and g are the density of the working fluid and the gravitational acceleration. To improve the accuracy of the results, an offset between the two pressure sensors was used for correction. The offset was determined with the test bench switched off: the valves between the pressure tube and the environment were opened and the water drained from the tube to ensure ambient pressure at all sensor positions. In this state, the measured pressure difference between the upper and lower sensors was 0.0026 bar.

Furthermore, a plausibility check was performed: The tube at ambient temperature was filled with water at a temperature of 75 °C starting from the bottom. Fig. 5 (left) shows the sudden temperature increases from levels L1 (red) to L5 (orange) at the points in time when the water level reaches the corresponding sensor position. Fig. 5 (right) compares the fill levels calculated based on the pressures (L(p)) at the time of the temperature rise using Eq. (1) with the measured heights of the sensor positions (L(T)). A maximum deviation for the complete 1.2 m length of the test section of 0.025 m was found. Considering a possible drift in the pressure sensor readings of 0.00684 bar during operation, this results in a maximum total deviation in the fill level of 0.033 m, which corresponds to a relative deviation of 3 %. In Figs. 7 and 8, this deviation is indicated by uncertainty bands.

2.2.3. Estimating the liquid fraction in the PCM

The liquid fraction f of the PCM is correlated linearly to the temperature of the PCM as defined in Eqs. (4)–(6):

$$\text{For } T_{PCM,sol} < T_{PCM} < T_{PCM,liq}: \quad f = \frac{T_{PCM} - T_{PCM,sol}}{T_{PCM,liq} - T_{PCM,sol}} \quad (4)$$

$$\text{For } T_{PCM} < T_{PCM,sol}: f = 0 \quad (5)$$

$$\text{For } T_{PCM} > T_{PCM,liq}: \quad f = 1 \quad (6)$$

$T_{PCM,sol}$ is the solidus and $T_{PCM,liq}$ the liquidus temperature of the PCM and T_{PCM} the mean temperature of the respective storage volume. This correlation is used as an approximation; it may not be accurate for phase change processes under all conditions. For the determination of the liquidus and the solidus temperature as well as for further discussion refer to Dietz et al. [15].

2.2.4. Design of experiments

In Table 3, the details of all experiments which were performed with the setup are summarised. They are designed to test the feasibility and effectiveness of optimised operating strategies based on mass flow rate and pressure variations of the HTF.

Fig. 6 gives a graphical overview of the settings for the HTF flow. The x-axis represents the mass flow rate, the left y-axis represents the pressure, and the right y-axis represents the corresponding saturation temperature of the HTF. All charging experiments and the melting range are marked in shades of red while all discharging experiments and the solidification range are marked in shades of blue.

Charging was performed for three different pressures and mass flow rates. The two upper pressure stages at 4.5 bar and 6.7 bar are suitable for the complete melting of the PCM due to their sufficiently high saturation temperatures. At 3.0 bar, only partial charging is possible.

Discharging was performed for two different pressures and three different mass flow rates. Fig. 6 shows that all implemented pressures lie within the solidification range which means that in none of the experiments complete solidification was achieved. This is due the PCM showing a lower solidification temperature (101 °C) than expected based on the information from the material datasheet. A detailed discussion of the melting and solidification behaviour, including the aspects such as hysteresis, cycling and DSC results, and the supplier information are provided in Dietz et al. [15]. The lowest pressure possible in the test rig is 1.4 bar with a saturation temperature of 109 °C. Lower pressures are instable in the fluid cycle due to their proximity to the ambient pressure. This implies that the discharging experiments are mainly performed as sensible processes. For the mass flow rate variation, higher mass flow rates are set for the lower pressure stage at 1.4 bar compared to the higher-pressure stage at 1.7 bar. The reason for this is the technical limitation of the heating power necessary to preheat the HTF flow to a defined temperature before it enters the test rig from the bottom. As the lower pressure stage requires a lower inlet temperature for identical subcooling, a higher mass flow rate can be preconditioned under these operating conditions. Thus, the present article focuses mainly on the charging process.

Arrows on the left side and at the bottom of the diagram indicate the expected trends for the size of the dominant heat transfer surface (DHTS), the storage power ($\dot{Q}_{stor}$), the process duration (*t*) and the total capacity of the storage. The dominant heat transfer surface refers thereby to the size of the heat exchange surface where the dominant proportion of the total power is transferred. According to Dietz et al. [14], the DHTS and $\dot{Q}_{stor}$ increase with increasing mass flow rate ($\dot{m}_{HTF}$).

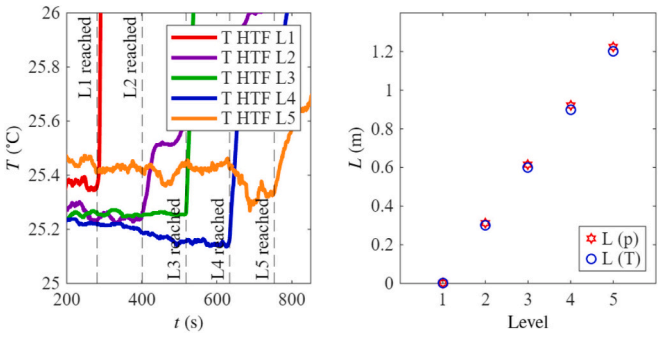

Fig. 5. Temperatures at levels L1 to L5 during plausibility check (left) and comparison of estimated fill levels L(p) and measured fill levels L(T) (right).

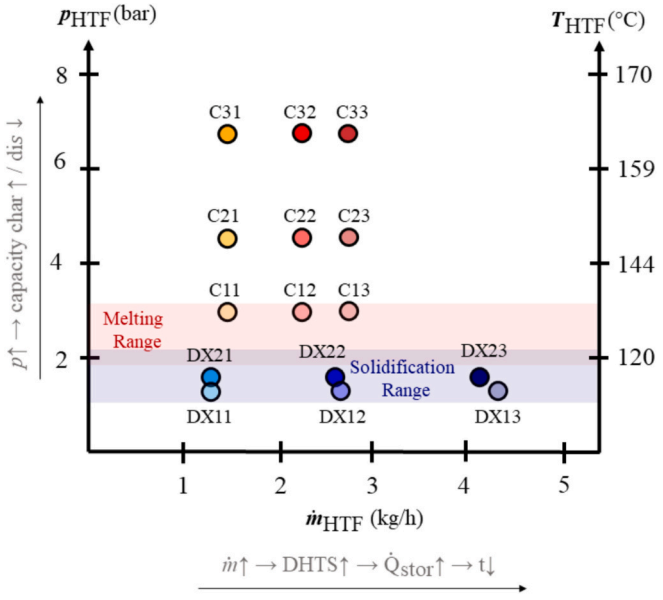

Fig. 6. Graphical representation of the design of experiments and expected main trends (C = Charging; D = Discharging).

If the capacity of the storage remains constant, t decreases consequently. The capacity of the storage element during charging is expected to increase, while during discharging it is expected to decrease by increasing pressures (and temperatures) of the HTF.

2.2.5. Quality of experimental results

The reference test C31 was repeated three times to verify the repeatability of the boundary conditions and results. The repetitions include measurements from the 21st and 44th cycles and thus also take into account possible cycle effects; the results are published in Appendix II in Dietz et al. [15]. For all other operating points, the tests were carried out once or twice.

2.2.6. Storage performance metrics

To clearly report the thermal performance dynamics of the storage, several parameters were defined and calculated based on experimental data generated by the storage. The metrics are defined as follows:

Charging/discharging time: $t_{char/dis} = t \mid 0 \leq x(t) \leq 1$, where:

- $t_{char/dis}$ = charging or discharging time [s]
- $x(t)$ = steam content in the storage at time t [dimensionless, with $0 \leq x(t) \leq 1$]

Theoretical storage capacity: $Cth = m_{PCM}\left(c_{p,PCM}\left(T_{PCM,end} - T_{PCM,start}\right) + \Delta h_{PCM}\right) + \quad m_{tubes}c_{p,tubes} \quad \left(T_{tubes,end} - T_{tubes\,start}\right) + \quad m_{fins}c_{p,fins}\left(T_{tubes,end} - T_{tubes,start}\right)$,where:

- C_{th} = theoretical storage capacity [Wh]
- m_{PCM}, m_{tubes}, m_{fins} = masses of PCM, tubes and fins [kg]
- $c_{p,PCM}$, $c_{p,tubes}$, $c_{p,fins}$ = specific heat capacities of PCM, tubes and fins [J/(kg K)]
- $T_{PCM,start}$, $T_{tubes,start}$, $T_{fins,start}$ = mean temperatures of PCM, tubes and fins at the beginning of the experiment [°C]
- $T_{PCM,end}$, $T_{tubes,end}$, $T_{fins,end}$ = mean temperatures of PCM, tubes and fins at the end of the experiment [°C]
- Δh_{PCM} = phase change enthalpy of the PCM [J/kg]

Effective storage capacity: $C_{eff} = \frac{C_{meas,end}}{C_{th}} \mid 0 \leq C_{eff} \leq 1$, where:

- C_{eff} = effective storage capacity [dimensionless, with $\mid 0 \leq C_{eff} \leq 1$]
- $C_{meas,end}$ = measured storage capacity that was effectively used for evaporation or condensation of the HTF until the end of the experiment [Wh]
- C_{th} = theoretical storage capacity [Wh]

Degree of charging/discharging: $DoC(t) = \frac{C_{meas}(t)}{C_{th}} \mid 0 \leq DoC(t) \leq 1$, where:

- $DoC(t)$ = Degree of charging/discharging at time t [dimensionless, with $\mid 0 \leq DoC(t) \leq 1$]
- $C_{meas}(t)$ = Measured used storage capacity at time t [Wh]
- C_{th} = theoretical storage capacity [Wh]

Relative power: $\dot{Q}_{stor,rel} = \frac{\dot{Q}_{stor,section}}{\dot{Q}_{stor,total}} \mid 0 \leq \dot{Q}_{stor,rel}(t) \leq 1$, where:

- $\dot{Q}_{stor,rel}$ = relative storage power [dimensionless, with $\mid 0 \leq \dot{Q}_{stor,rel}(t) \leq 1$]
- $\dot{Q}_{stor,section}$= absolute storage power in a single storage section [W]
- $\dot{Q}_{stor,total}$= absolute total storage power [W]

Besides these metrics, the following terms are used as defined below:

- *Storage*: Unit consisting of PCM, tubes and fins.
- *Full load storage operation*: Operating mode in which HTF changes phase along the entire length of the tube (compare radial fronts).
- *Partial load storage operation*: Operating mode in which HTF changes phase along parts of the tube length (compare axial fronts).

3. Experimental results and discussion

This section presents a selection of experiments from Table 3 (Annex I) to illustrate the core findings of the investigation, focussing on the charging experiments. The systematic experimental analysis of the LH-TES element contributes to fundamental knowledge for practical system integration of once-through PCM storage. It includes precise control of the HTF parameters and detailed monitoring of the storage for the quantitative analysis of control strategies with focus on optimising power control and efficient PCM utilisation.

Section 3.1 presents the transient power profiles of the storage and the liquid levels in the pressure tube for mass flow rate and pressure variations of the HTF during charging and discharging. The focus of Section 3.2 is the local temperature distribution in the storage during charging and Section 3.3 shows the local heat transfer and the local liquid fraction in the PCM for different mass flow rates and pressures, also for the charging process.

3.1. Power and liquid level

3.1.1. Variation of the mass flow rate of the HTF during charging

Firstly, the influence of the variation of the HTF mass flow rate on the transient charging power profile of the storage and on the HTF liquid level in the tube is investigated. Fig. 7 (left) shows the results for the charging experiments C31, C32 and C33 with different mass flow rates of 1.44 kg/h (green), 2.16 kg/h (red) and 2.88 kg/h (blue), in which the initial temperature of the storage was 105 °C and the pressure of the HTF was set to 6.7 bar which corresponds to a saturation temperature of 163 °C.

The thick lines in dark green, red and dark blue represent the storage power over time and the areas coloured transparently in the same colour indicate the corresponding areas of uncertainty. Initially, the peak powers for 1.46 kg/h, 2.19 kg/h and 2.88 kg/h are 938 W, 1406 W and 1842 W respectively. This corresponds to a directly proportional correlation between the mass flow rate of the HTF and the storage power and thus enables precise power adjustment.

For the experiment with the highest mass flow rate, the approximately constant power plateau drops first after 8.0 min, followed by the plateau for the medium mass flow rate after 11.9 min and the plateau of the lowest mass flow rate after 19.5 min. On the one hand, this is caused by the higher power due to higher mass flow rates, which result in faster charging and therefore shorter charging times for a constant storage capacity. However, the degree of charging at the time of the power drop also increases with decreasing mass flow rates. It is 62 % for 2.88 kg/h, 70 % for 2.16 kg/h and 77 % for 1.44 kg/h, which means that 242 Wh, 272 Wh and 299 Wh respectively were transferred by the end of the process. Consequently, the effective capacity of the storage increases as the mass flow rate decreases, further extending the charging time.

The fine lines in Fig. 7 in light green, orange and light blue show the transient liquid level in the pressure tubes and in this way indicate the phase change boundary in the HTF tube. The corresponding uncertainty bands are marked with transparent lines of the same colour. At high mass flow rates, this boundary moves down the tube earlier, which implies that the axial position of the condensation and thus the location of the intensive heat transfer moves faster through the tube and then exits earlier at the lower end of the system boundary. The power drops from the highest to the lowest mass flow rate at filling levels of 0.41 m, 0.51 m and 0.35 m (circles in Fig. 7). This behaviour is confirmed by the results of experiments C11, C12 and C13 in Fig. 7 (right). They have been performed with a pressure of 3.0 bar instead of 6.7 bar in the HTF flow under otherwise identical conditions.

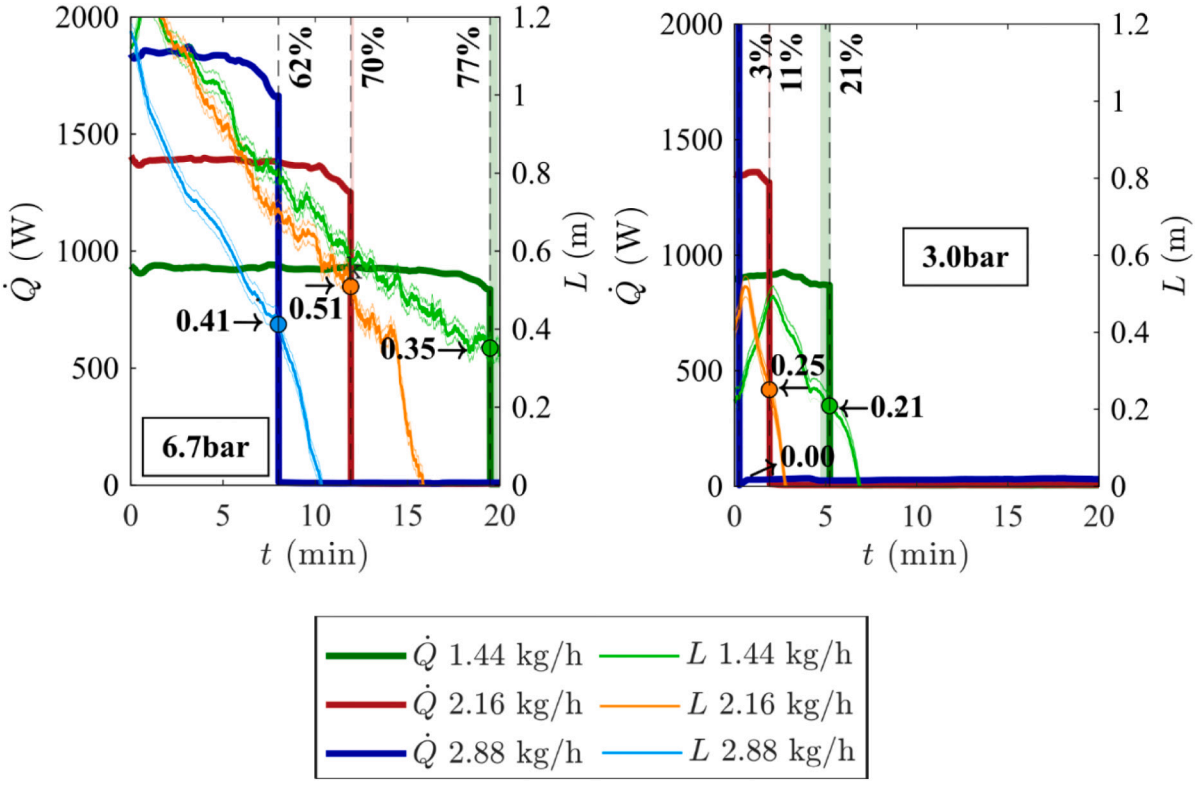

Fig. 7. Transient charging power (bold lines) with uncertainty range, corresponding HTF liquid levels (fine lines) with uncertainty bands and corresponding degrees of charging at the ends of the plateaus of constant power for C31, C32, C33 (left) and C11, C12, C13 (right).

In addition, at a mass flow rate of 2.88 kg/h, the power drops to zero shortly after the start of the experiment at a degree of charging of only 3 %, with the amount of energy transferred up to that point amounting to 9 Wh. It can be concluded that the fin performance is not sufficient under these operating conditions: Although the storage is still discharged to a large extend and the power provided by the HTF flow is high, it is not possible to achieve a sufficient power density to condensate the HTF within the system boundary. The more the fins enhance heat transfer in the PCM, the higher is the effective heat capacity of the storage from a design point of view.

The parameter study results at the single-tube setup show that the mass flow rate – not only in theory but also in practice – is an effective parameter to adjust the storage power and to increase the effective capacity of the storage, which is crucial for power control and efficient utilisation of the PCM. They confirm the results of earlier exemplary studies for larger multi-tube storage systems on the relationship between the mass flow rate of the HTF and the storage power [10]. The demonstrated increase in effective capacity at lower mass flow rates is a new finding that has not yet been reported. Furthermore, the results of this publication on the liquid level illustrate the movement of the local condensation and demonstrate the limits of the utilised fins for high mass flow rates.

3.1.2. *Variation of the pressure of the HTF during charging*

This second section focuses on the influence of the variation of the HTF pressure on the transient charging power profile of the storage and on the HTF liquid level in the tube. Fig. 8 shows the results for the charging experiments C11, C21 and C31 with different pressures of 3.0 bar (green), 4.5 bar (red) and 6.7 bar (blue), in which the initial temperature of the storage was 105 °C and the mass flow rate of the HTF was at 1.44 kg/h. The corresponding saturation temperatures are 134 °C, 148 °C and 163 °C respectively.

With a pressure variation, the effective capacities in relation to the capacity of the storage element for the highest HTF pressure level

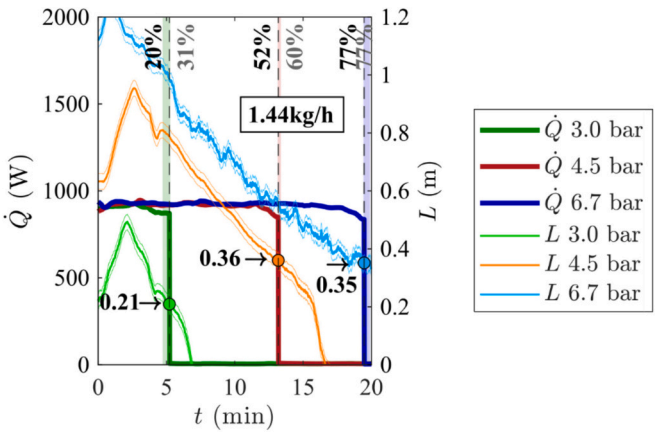

Fig. 8. Transient charging power (bold lines) with uncertainty range, corresponding HTF liquid levels (fine lines) with uncertainty bands and corresponding degrees of charging at the ends of the plateaus of constant power in relation to the respective theoretical capacities (grey) and the theoretical capacity for the maximum pressure level of 6.7 bar (black) for C11, C21 and C31.

increase with increasing pressure levels from 20 % to 52 % to 77 %, which means that 78 Wh, 202 Wh and 299 Wh respectively were transferred by the end of the process. This is to be expected due to the increase in sensible capacity with increasing temperature ranges. But also, the effective capacities relative to the respective capacity for the corresponding pressure level increase with increasing pressure from 31 % to 60 % to 77 %. This indicates that higher pressure levels and thus greater temperature differences between the HTF and the storage activate a larger proportion of the storage material.

The analysis of the pressure variation in the HTF during the charging process shows that not only reducing the mass flow rate but also

increasing the pressure of the HTF increases the effective capacity of LH-TES when operated with a two-phase HTF. This finding has not yet been published and can improve the utilisation of effective PCM material in LH-TES in practice.

3.1.3. *Variation of the mass flow rate and pressure of the HTF during discharging*

After discussing the charging results for transient storage power and effective capacity regarding HTF mass flow rate and pressure variations, this section offers a brief analysis of selected discharging results. Fig. 9 (left) shows the results for the discharging experiments D211, D212 and D213 with nominal mass flow rates of 1.26 kg/h (green), 2.78 kg/h (red) and 4.30 kg/h (blue). The initial temperature of the storage was 150 °C and the pressure of the HTF was at 1.4 bar which corresponds to a saturation temperature of 109 °C.

In analogy to the charging process, the peak powers of 938 W for 1.43 kg/h, 1820 W for 2.77 kg/h and 2841 W for 4.32 kg/h are directly proportional to the mass flow rate.

For technical reasons discussed in Dietz et al. [15], the end of the constant power plateaus and thus the effective capacities of the storage cannot be determined for discharging. Nevertheless, the degree of discharging increases with decreasing mass flow rates from 17 % to 19 % to 46 % up to the point at which the HTF changes from the gaseous state to the two-phase state at the outlet, which means that 68 Wh, 80 Wh and 189 Wh respectively were transferred by this time. Furthermore, the results for the experiments D221, D222, D223 with an HTF pressure of 1.7 bar instead of 1.4 bar in Fig. 9 (right) show degrees of discharge of 15 %, 20 % and 30 %, which means that 58 Wh, 82 Wh and 124 Wh respectively were transferred by this time. Accordingly, increasing the pressure of the HTF and thus reducing the temperature difference between the storage and the HTF reduces the degree of discharging. As the pressure variation is small, the results are not as clear as for the charging process.

Overall, also the discharging results confirm the directly proportional correlation between the mass flow rate of the HTF and the storage power.

3.2. *Axial and radial temperature distribution in the storage during charging*

To examine the local behaviour of the storage during charging in more detail, the axial and radial temperature distributions in the storage are discussed in this section.

The diagrams in Fig. 10 on the top show the transient temperature profiles in the HTF (solid lines) and in the PCM (dashed lines) on the five measurement levels L1 (bottom, blue) to L5 (top, red) as well as the saturation temperature of the HTF (Tsat HTF), the liquidus temperature (Tliq PCM) and solidus temperature (Tsol PCM) of the PCM and the time t1 at which the HTF on L3 reaches saturation temperature. The diagrams below indicate the corresponding axial (horizontal arrangement) and radial (vertical arrangement) temperature profiles in the PCM (blue) and the axial temperature profile in the HTF flow (red) at the time t1. Arrows represent the flow direction of the HTF.

Fig. 10 (centre) shows the reference case C31: The initial temperature of the storage is 105 °C and the HTF flow enters from the top of the tube with a pressure of 6.7 bar and a mass flow rate of 1.44 kg/h. After 6.8 min, the HTF flow at L3 reaches saturation temperature. At this point, the maximum axial and radial and temperature gradients in the PCM are 49 K and16 K respectively. At L2, the PCM still has an initial temperature of approximately 105 °C, from L3 it begins to heat up. The reason for this is the small temperature difference between the storage and the HTF flow on levels L1 and L2. There is a large temperature change of 56 K in the HTF flow between L2 and L3, which significantly increases the driving temperature difference between flow and storage from L3 upwards and thus enables heat transfer on levels L3 to L5. This driving temperature difference then decreases from L3 to L5 from 45 K to 21 K to 12 K. From L3 to L4, the radial temperature spread in the PCM increases as the heating process progresses from a low initial temperature. This is due to a combination of a high-power rate, driven by the large temperature difference between the storage and the flow, and the radial heat transfer resistance in the storage. The spread then decreases again from L4 to L5 with the storage approaching its equilibrium temperature.

Fig. 10 (left) shows the results of C33 with a mass flow rate of 2.88 kg/h instead of 1.44 kg/h. The HTF reaches saturation temperature on L3 after 1.2 min with maximum axial and radial temperature gradients in the PCM of 17 K and 3 K respectively. As in the reference experiment C31, the large temperature change of 52 K in the HTF flow between L2 and L3 enables the storage to be heated from L3 upwards. The driving temperature difference between the flow and the storage decreases only slightly from L3 to L5 from 53 K to 47 K to 46 K.

Fig. 10 (right) shows the results for C11 with a pressure of 3.0 bar instead of 6.7 bar. The HTF reaches saturation temperature simultaneously on L2 and L3 after 2.5 min with maximum axial and radial temperature gradients in the PCM of 14 K and 3 K respectively. The temperature change of 22 K in the HTF flow between L1 and L2 enables the heating of the storage from L2 upwards. Unlike in the previous cases, the driving temperature difference between the flow and the storage does not decrease from L2 to L5.

In general, the temperature distribution in the storage represents firstly the amount of thermal energy – the product of charging time and power – that has been transferred since the initiation of the process, and

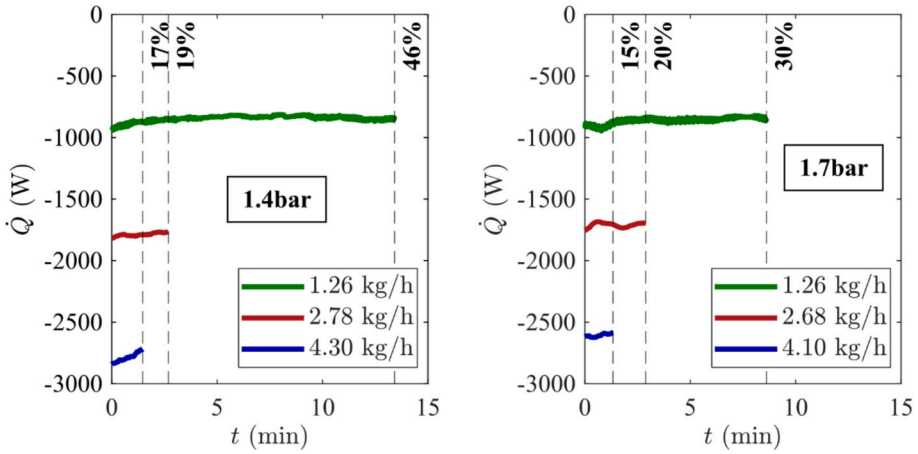

Fig. 9. Transient discharging power and corresponding degree of discharging until the HTF exits two-phase at the outlet of the storage for D211, D212, D213 (left) and D221, D222, D223 (right). Minor uncertainty areas not visible.

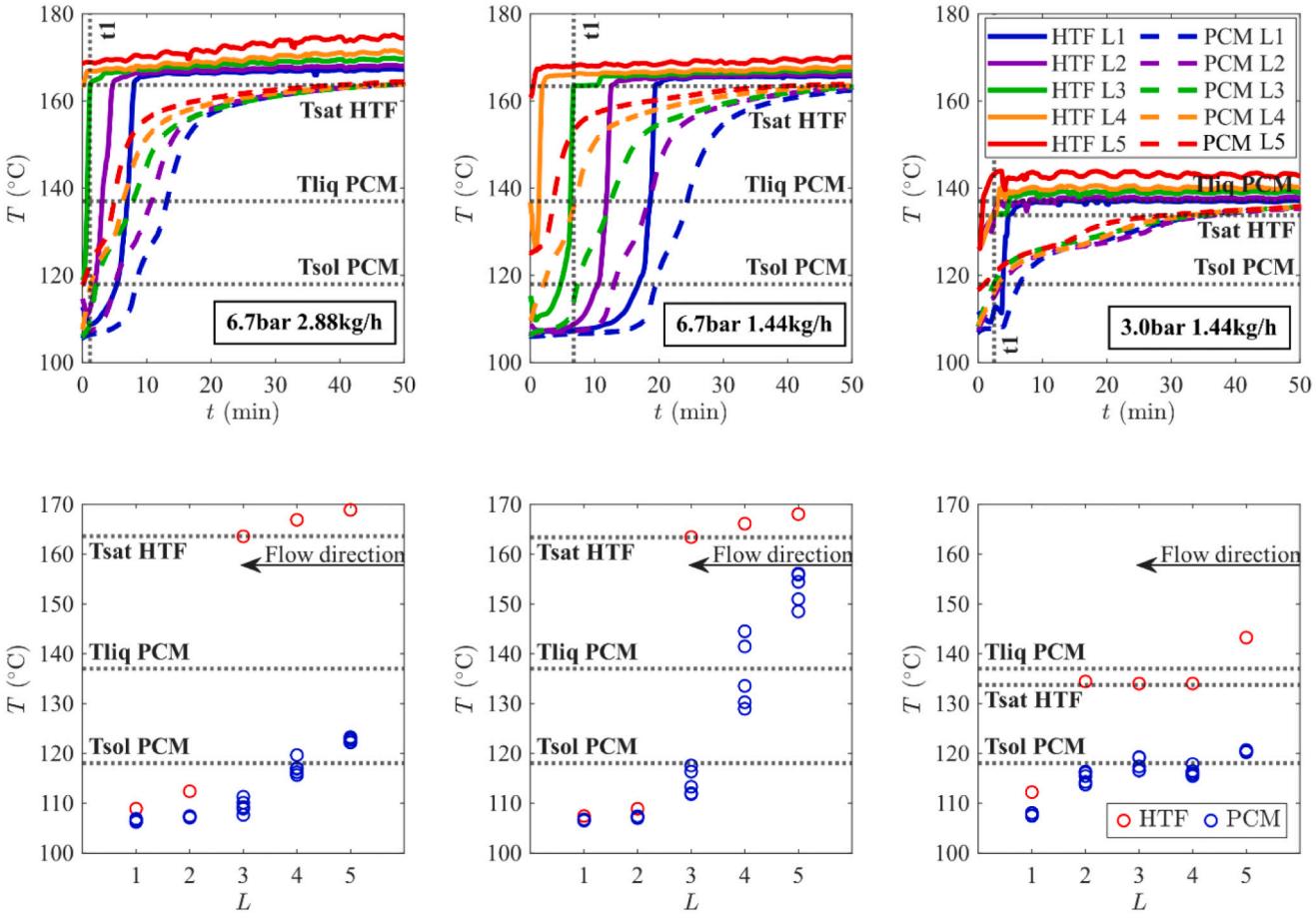

Fig. 10. Top: Transient temperature profiles in the HTF and in the PCM and indication of time t1 for C33 (left), C31 (centre) and C11 (right, legend). Bottom: Corresponding axial and radial temperature distribution in the PCM (blue) and axial temperature distribution in the HTF (red) at t1. (For interpretation of the references to colour in this figure legend, the reader is referred to the web version of this article.)

secondly the local distribution of thermal energy in the storage. High storage temperatures represent large quantities of transferred thermal energy, while high gradients indicate that the thermal energy has been distributed unevenly in the storage due to thermal resistance.

The results in this section therefore show that at the time when the storage tube is filled up to level L3 with gaseous HTF, the amount of thermal energy transferred is highest in the reference case C31, as the storage temperatures are highest in this case. The lower power rate compared to experiment C33 with the higher mass flow rate is compensated for by the long time required for the flow to reach the saturation temperature at L3.

In addition, the reference case has the most uneven temperature distribution in the axial and radial direction. Compared to the case with lower pressure C11, the temperature difference between the initial temperature and the saturation temperature of the HTF is large and compared to the case with higher mass flow rate C33, the flow takes longer to reach the saturation temperature on L3, which means that the charging process is already further advanced.

As a result, it can be concluded that increasing the mass flow rate and decreasing the pressure of the HTF lead to a more homogeneous distribution of the transferred thermal energy in axial direction of the storage and thus a less pronounced temperature stratification. At the same time, the movement of the condensation area in the tube from the top to the bottom of the storage is accelerated. An analysis of the HTF/PCM interaction with the level of detail of this study is not known to the authors of this work.

3.3. *Local heat transfer and local liquid fraction of the PCM during charging*

Based on the temperature measurement network in the PCM and in the HTF flow, conclusions can be drawn on the local heat transfer in individual sections of the storage container. Fig. 11 presents the power in the storage sections S12 (blue), S23 (pink), S34 (orange) and S45 (red) in relation to the total storage power $\dot{Q}$(norm) (grey) as well as the liquid fraction of the PCM f (dashed lines) in the corresponding sections.

In analogy to Section 3.2, the reference case in Fig. 11 (centre) is C31: The initial temperature of the storage is 105 °C and the HTF flow enters from the top of the tube with a pressure of 6.7 bar and a mass flow rate of 1.44 kg/h.

For these conditions, the area of high-power density clearly moves from top to bottom through all four sections. It passes through S45 in 1.8 min, S34 in 6.6 min, S23 in 4.3 min and S12 in 6.8 min. The relative power in a section is always greater than 0.88, which indicates that only little thermal energy is transferred outside the area with high power density, the storage tank is passive there. This leads to a strongly axial charging process with pronounced axial temperature stratification, as described in Section 3.2. The melting process in the sections begins and ends with a time delay and continues even when no more thermal energy is transferred. This indicates conductive heat transfer from outside the system boundary and the redistribution of thermal energy in the storage tank, as discussed in detail in Dietz et al. [15].

Fig. 11 (left) shows the results for C33 with a mass flow rate of 2.88 kg/h instead of 1.44 kg/h. In this case with increased mass flow rate, the charging process is also axial, but the high-power area moves faster,

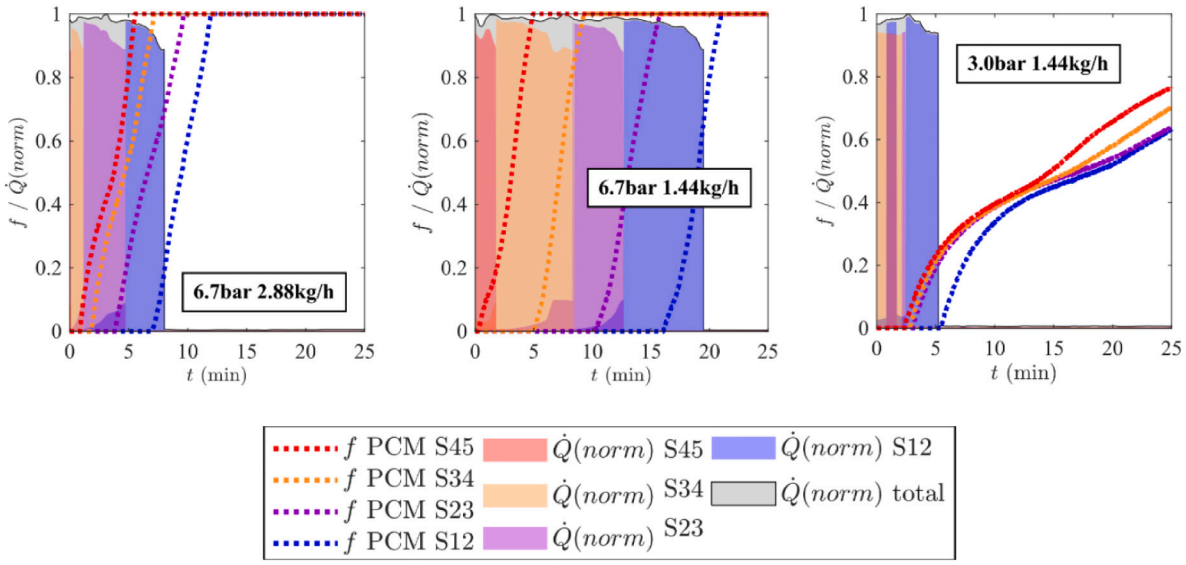

Fig. 11. Relative power in the storage sections S12, S23, S34 and S45 as well as the liquid fraction of the PCM in the corresponding sections for C33 (left), C31 (centre) and C11 (right).

passing through S34 in 1.2 min, through S23 in 3.5 min and through S12 in 3.3 min. As in the reference case, the relative power in a section is always more than 0.88. The time offset between the end of the heat transfer in one section and the completion of the melting process in the same section is larger compared to the reference case C31, which means that a greater proportion of the storage volume within the system boundary is charged by redistributing thermal energy and by heat sources outside the system boundary.

Fig. 11 (right) shows the results for C11 at a pressure of 3.0 bar instead of 6.7 bar. In this case with reduced pressure, the charging process is less axial compared to the reference case C31 and the case with varied mass flow rate C33. The heat transfer takes place simultaneously in all sections. Nevertheless, a clearly radial charging behaviour cannot be demonstrated, as this would require similar relative powers on all levels over the entire charging process. The time lag between the end of the heat transfer in a section and the completion of the melting process in the same section is as great that the melting process only begins after the heat transfer in the system boundary has already stopped.

The analysis of the local heat transfer and the local liquid fraction in the storage element proves axial charging for low mass flow rates and high pressures. It shows that only parts of the storage element are actively involved in the heat transfer, and the clear demarcation between the active and passive areas is also evident. This means that the location of the heat transfer in the PCM storage can be defined by specifically controlling the pressure and mass flow rate of the HTF. Previous publications [7,8] reported on the temperature distribution in the storage tank and estimated the liquid fraction of the PCM based thereon. Furthermore, Laing et al. [16] estimated the local flow temperatures from temperature measurements at the outside of the tubes. However, without the measurement of the exact temperatures and pressures of the HTF along the tube, it is not possible to obtain reliable information on the local flow conditions and based thereon derive the power rate for single sections of the tube.

4. Comparison of experimental and numerical results

To contribute to a fundamental understanding of the practical system integration of PCM storage, this section evaluates the numerical model used for the design of the test rig, introduced in Dietz et al. [15].

The aim of the model is to provide computationally efficient, realistic and transient solutions for shell-and-tube LH-TES with coupled HTF and storage area to perform parameter variations for design purposes. Therefore, it should allow the prediction of transient power profiles, transient outlet temperatures of the HTF as well as charging and discharging times. Optionally, knowledge of the axial temperature distribution in the storage and the liquid fraction of the PCM is also valuable.

The model consists of a 1d HTF model coupled with a 2d storage model for the PCM volume with integrated fins.

Regarding the discussions in this article, the following assumptions are most relevant:

- The boundaries of the PCM volume are adiabatic.
- Natural convection in the storage tank is neglected, only heat conduction is considered.
- The thermal contact resistances between the tube and the aluminium fins and between the fins and the PCM are neglected.
- A linear correlation between the temperature and the liquid fraction of the PCM according to Eq. (4) is assumed.

A detailed description of the model can be found in Annex II.

In this article, a graphical method is used for validation: The experimental data for the storage power, the process duration, the outlet temperature of the HTF and the axial temperature distribution in the storage from the single-tube test rig described in Section 2.1 are plotted against the results from the model for the simulated experiments. For this purpose, the transient boundary conditions – pressure, temperature and mass flow rate of the HTF – are linearly interpolated and implemented in the model configuration. In addition, an arithmetic mean temperature based on the measured temperatures in the storage is used as the initial storage temperature for the simulation. Fig. 12 shows a graphical overview of the input and output parameters of the model.

Deviations are determined and discussed, and the suitability of the model is derived. The corresponding measurement uncertainties of the experimental data have been discussed in detail by Dietz et al. [15].

4.1. Transient power profiles and HTF outlet temperatures during charging

Firstly, the most important model outputs for storage design are discussed: the transient power profiles with the corresponding charging times and the HTF outlet temperatures.

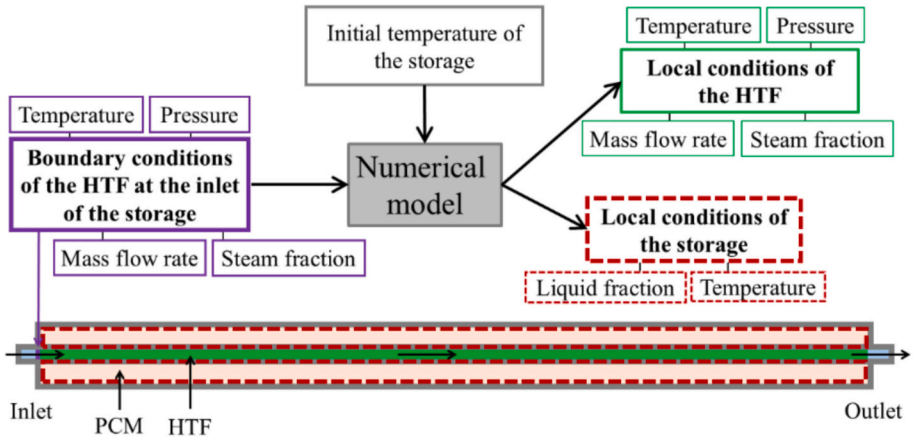

Fig. 12. Model input parameters (boundary and initial conditions) and model output parameters (local conditions of the HTF and the storage) for a storage element.

Fig. 13 (a) shows the experimentally determined (e, solid lines) and the simulated (s, dashed lines) storage powers for experiments C31, C32 and C33. For these cases, the initial temperature of the storage is approximately 105 °C and the HTF flow enters from the top of the tube with a pressure of 6.7 bar. The mass flow rate is varied from 1.44 kg/h to 2.16 kg/h to 2.88 kg/h. The phase change in the PCM begins for all cases after <0.5 min.

For all three cases, the peak power can be predicted by the model with deviations of the maximum power values of <3 %.

For the first 18.6 min, 10.9 min and 7.3 min for 1.44 kg/h, 2.16 kg/h and 2.88 kg/h respectively, the experimental storage power is slightly higher compared to the simulated power – apart from fluctuations at the very beginning of the experiments. Fig. 13(b) shows how this affects the HTF outlet temperatures at the bottom of the storage: As the HTF releases more thermal energy to the storage in the experiment, it is also more subcooled at the outlet. The effect is amplified by the low mass

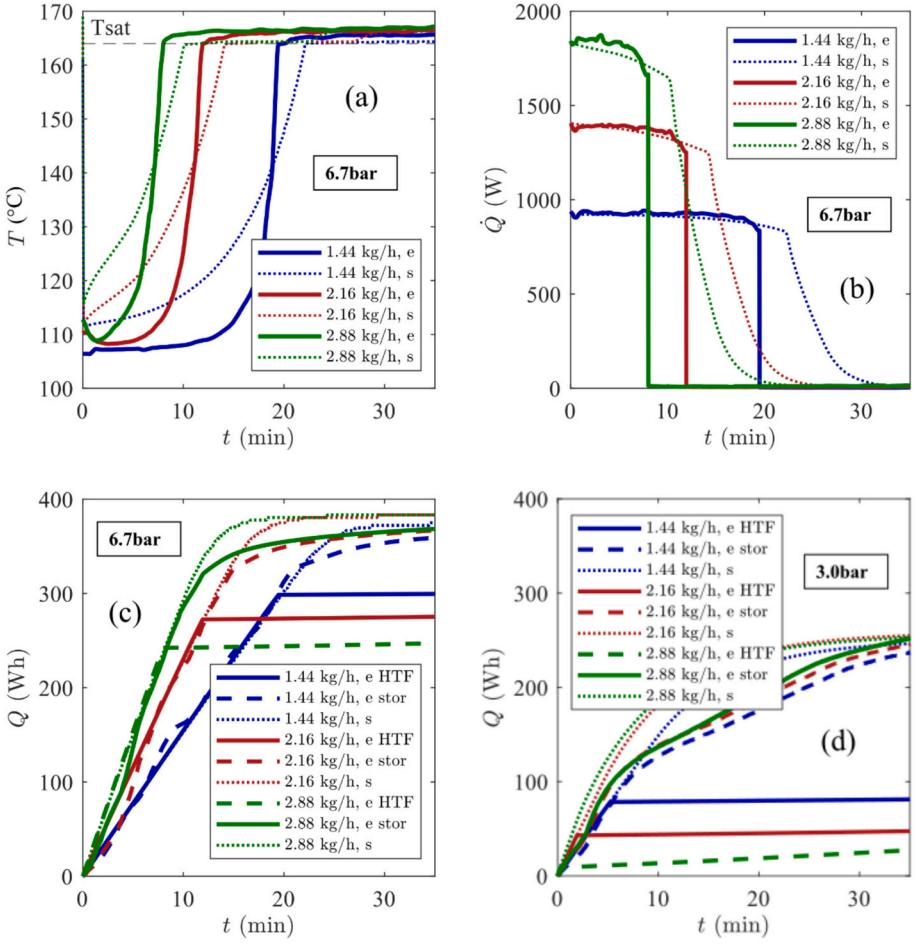

Fig. 13. Comparison of experimental (e) and simulation (s) results for the transient power profiles (a), the outlet temperatures of the HTF (b) and the cumulative transferred thermal energy for C31, C32, C33 (c) as well as the cumulative transferred thermal energy for C11, C12, C13 (d). *HTF* means based on the HTF balance, *stor* means based on the storage balance as defined in Section 2.2.1.

flow rates of the HTF. This behaviour may be caused by the non-adiabatic nature of the real system: Outer parts of the test section as the base plate of the storage or the HTF tube have low temperatures at the beginning of the experiments and are heated by the flow via heat conduction across the system boundary. They act as heat sinks outside of system boundary under consideration. As a result, more thermal energy is transferred from the flow to the surrounding test rig in the experiment.

For later times, the experimental plateaus of almost constant power drop 2.6 min, 2.2 min and 2.3 min earlier compared to the simulation results for 1.44 kg/h, 2.16 kg/h and 2.88 kg/h which corresponds to 28 %, 18 % and 13 % of the complete experimental plateaus. These are the times at which the HTF flow at the outlet system boundary changes from the subcooled to the saturated state. This means that it can no longer be fully condensed within the system boundary. While the simulated power profiles slowly decrease over a period of 14.1 min, 12.9 min and 12.6 min, the experimental results show a sudden drop in power within only one second. These time periods in the simulation correspond to the phase change time of the HTF: the simulated HTF outlet temperatures remain at saturation temperature while the steam content in the flow increases. In the experiment, the HTF flow superheats almost immediately after reaching saturation temperature. These observations show that for later times, the experimental storage power is lower compared to the simulated power. Consequently, the outlet temperature of the HTF rises faster in the experiment as less thermal energy is dissipated from the HTF flow. This is also caused by non-adiabatic conditions: As described in Dietz et al. [15], condensation continues below level L1 after it has already stopped in the considered storage section above. The transferred thermal energy in this lower section is then channelled across the system boundary and continues to charge the storage without the HTF supplying thermal energy. This also could indicate the increase in radial resistance over time.

Fig. 13(c) shows the cumulative thermal energy transferred since the start of the experiments. It corresponds to the integrated storage power over time. In addition to the experimental results based on the HTF balance (e HTF, solid lines) and the simulative results (s, fine dashed lines), it includes the experimental results based on the storage balance (e stor, dashed lines) as described by Eq. (2). The experimental profiles based on the HTF balances stagnate after 19.5 min, 11.9 min and 8.0 min for 1.44 kg/h, 2.16 kg/h and 2.88 kg/h due to heat transfer from outside the system boundary as described in the previous paragraph. Thus, they cannot be used for comparison with the simulation data from this point onwards. Instead, the experimental results based on the storage balance are used.

At the end of the experiment, the final value for the transferred thermal energy based on the storage balance is higher in the simulation than in the experiment for all three cases. Fig. 13(d) shows the results for the cumulative thermal energy for experiments C11, C12 and C13 under identical conditions, but with an HTF pressure of 3.0 bar instead of 6.7 bar. In this case, the final temperatures in the experiment and in the simulation are more similar. This suggests that the deviation in the high-temperature test at 6.7 bar is due to heat losses from the small test rig with a high surface-to-volume ratio to the environment.

As outlined in the Section 2.2.4, the experimental data from this study are unsuitable for validating the simulation of the discharging process, as the PCM fully solidifies only at 101 °C, significantly lower than the value reported in its datasheet. This deviation, discussed in detail in the authors' previous work [15], reflects the material's actual melting and solidification behaviour under practical conditions.

The comparison of experimental and simulated results shows that the peak power during charging can be accurately predicted by the model. Furthermore, the transient power profiles and the outlet temperatures of the HTF are sufficiently accurate to be used reliably for design purposes – the longer the process under consideration, the lower the relative deviation between the experimental and the simulation results. The effects of heat sources and heat sinks surrounding the storage must be considered.

4.2. Axial temperature stratification and liquid fraction in the storage during charging

This section compares the simulated and experimentally calculated state of charge, described by the temperature and liquid fraction of the PCM.

Knowledge of the temperature gradients in the storage tank can support the risk assessment as early as the planning phase. By estimating the maximum temperature differences, the model can support the calculation of thermal stresses, e.g. for the tubes and the PCM tank. Fig. 14 shows the measured (e, solid lines) and the simulated (s, dashed lines) temperatures on the storage on the levels L1 (blue, bottom) to L5 (red, top) in the temperature probe positions in Fig. 15 for C31 (a) and C11 (b) as well as the liquid fraction for the cases discussed in Section 4.1.

The initial storage temperatures differ for both pressure levels, as the model works with a uniform, averaged temperature. In addition, the shape of the melting plateaus is different for the simulated and the measured temperatures. This can be caused using approximated solidus and liquidus temperatures and/or the different integration of the linear model for the liquid fraction. In the experiment, the temperatures are measured, and the liquid fraction is derived based on the linear correlation described in Section 2.2.3. For the simulation, on the other hand, the temperature of a cell is calculated based on the energy content and the material properties used in the case configuration. A comparison of the measurement-based and simulated liquid fraction is shown in Fig. 14 (c) for a pressure level of 6.7 bar and (d) for a pressure level of 3.0 bar. Mixing effects due to natural convection in the real system cannot be ruled out either, even if they are suppressed by the narrow geometry of the aluminium fins.

Fig. 14(a) shows deviations $5 < K$ between the experimental and the simulative data for the final storage temperatures at a pressure level of 6.7 bar. For the pressure level of 3.0 bar in Fig. 14(b), they are <1 K which indicates that they result from heat losses to the environment at high storage temperatures. These heat losses are reinforced by the small size of the test rig.

The model therefore allows an approximation of the axial temperature stratification in the storage tank, which can be important for the consideration of thermal stresses and possible damage caused by them. Since the small test setup was not completely adiabatic, the validity of the correlated model results for temperature profiles and liquid fraction cannot be proven. It is likely that the simulation of the liquid fraction in the PCM requires improvements in terms of the temperature correlation used and the melting behaviour assumed.

The validation results in this section indicate that a detailed knowledge of the material properties and the melting and solidification characteristics of the PCM, including the corresponding process dynamics, is required to improve the numerical model.

4.3. Transferability to multi-tube designs

This study aims to contribute to improving the design and operation of large-scale LH-TES based on a single tube study. Therefore, deviations can be expected when transferring the experimental and simulated findings to an actual multi-tube design.

Firstly, in practice, as the storage capacity increases, heat losses to the environment are inversely related to the storage size, as the ratio of surface area to volume decreases with increasing the storage dimensions. In this case, it is to be expected that this will lead to a better agreement between the simulation results under adiabatic assumptions. Secondly, however, in multi-tube systems, uneven distribution of the HTF from the header to the tubes is very likely, resulting in different positions and sizes of the DHTS in different tubes. This behaviour is not reflected in the model and therefore leads to increased uncertainties regarding the predicted storage behaviour. However, experiments by Theologou et al. [6] show that power control is still possible by varying

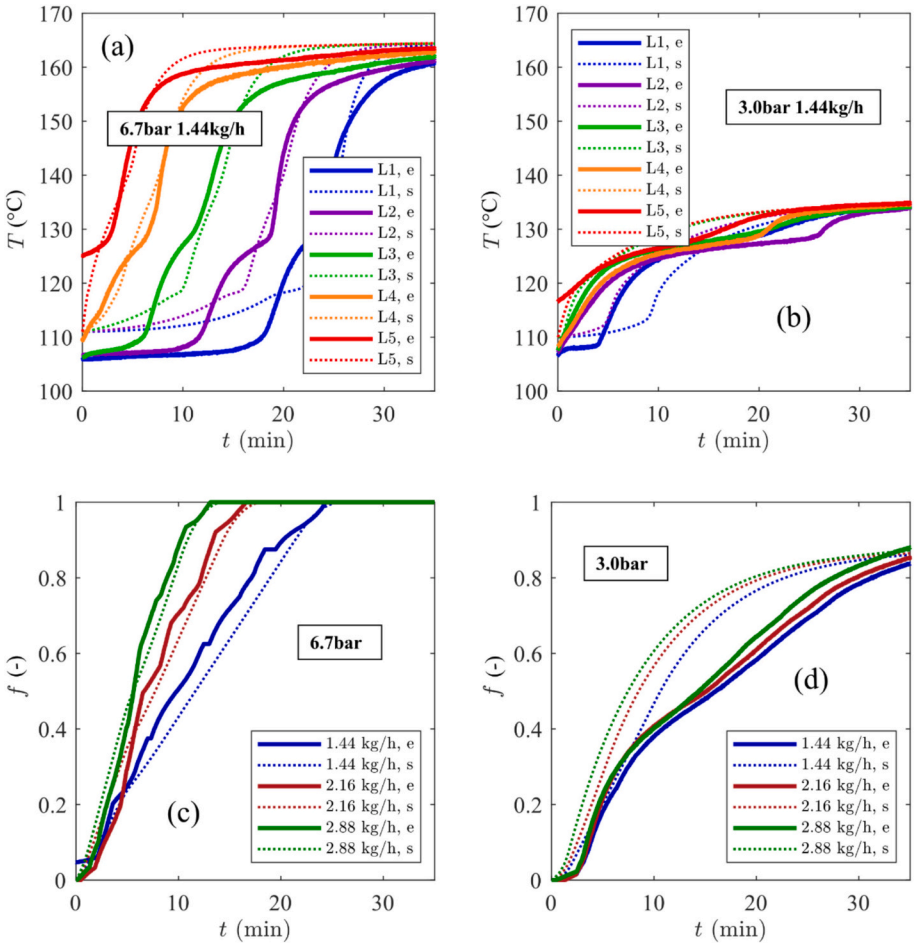

Fig. 14. Comparison of experimental (e) and simulation (s) results for the temperatures on measurement levels L1 to L5 for C31 (a) and C11 (b). Liquid fraction for C31, C32, C33 (c) and C11, C12, C13 (d).

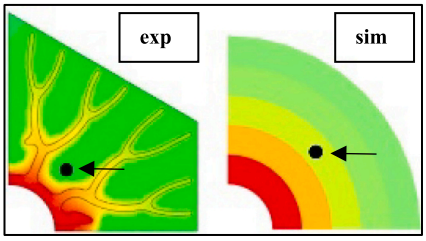

Fig. 15. Position of temperature probe in experiment (left) and simulation (right) [17].

the mass flow at an LH-TES with 56 tubes and a fill weight of 4450 kg of salt.

5. Summary and conclusions

For the quantitative analysis of control strategies for steam generation with intrinsically transient PCM storage, systematic experimental analyses with precise control of the HTF parameters and detailed monitoring of the storage are essential to improve the understanding of the PCM/HTF interaction and to validate simulation results. This work is intended to provide the first results of this kind for practical system integration.

The experimental results show that the mass flow rate of the HTF can be used as an effective parameter for adjusting the storage power due to a directly proportional correlation – not just theoretically, but also in real applications. This proof raises great practical potential: While at full load, the storage is charged in radial direction from the inside to the outside, axial charging is achieved at so-called partial load with reduced mass flow rates. Instead of a rapidly forming solidification layer over the entire heat transfer surface at full load, which restricts the heat transfer and reduces the storage power over time, at partial load parts of the heat transfer surface remain free until the end of the process and the transferable power remains constant over time.

Additionally, reduced mass flow rates significantly increase the effective capacity from 62 % to 77 % during charging. By increasing the pressure of the HTF during charging, the effective capacity can further be improved from 31 % to 77 %. Thus, a larger proportion of the available thermal energy can be dissipated by the end of the charging process.

Based on these findings, the design process and the decision on the arrangement of several storage modules (serial or parallel) for high-performance LH-TES for steam generation can be extended to partial-load, enabling controlled operation with cost-effective heat exchangers and improved material efficiency.

By comparing the experimental and the simulation results, it is found that the peak power for charging can be accurately predicted by the numerical model. With sufficiently long processes, also the transient power profiles and the outlet temperatures of the HTF can be used for efficient storage design.

Both the experimental and the simulative results of this work therefore enable cost optimisation of LH-TES and thus increase its marketability.

However, the analysis of the local PCM/HTF interaction as well as

the accuracy of the validation for the simulation model, are limited due to insufficient thermal decoupling of the small setup from the environment and limited knowledge on the phase change behaviour of the PCM.

Future research on practical system integration of PCM storage should focus on experimental setups with optimal thermal decoupling – especially for small test facilities – to improve the understanding of the HTF/PCM interaction and to generate high-quality measurement data for the validation of mathematical storage models. In addition, mathematical models for calculating the liquid fraction of the PCM must be further developed for the optimisation of design models. The basis for this should be extensive measurement data on the material-specific phase change behaviour of the PCM. In storage geometries that allow movement of the PCM, the effects of natural convection may also need to be considered for the charging process.

In summary, this study lays the foundation for utilising the effects of mass flow control in steam-driven LH-TES, starting from a specific operating range and storage geometry. The findings of this article can now be deepened by extending the operating range and investigating the transferability of the results to multi-tube storage systems.

CRediT authorship contribution statement

Larissa Dietz: Writing – original draft, Visualization, Methodology, Investigation, Conceptualization. **Michael Fiss:** Investigation. **Wolf-Dieter Steinmann:** Writing – review & editing, Conceptualization. **Inga Bürger:** Writing – review & editing, Supervision, Conceptualization. **Andrea Gutierrez:** Writing – review & editing, Supervision.

Declaration of competing interest

The authors declare that they have no known competing financial interests or personal relationships that could have appeared to influence the work reported in this paper.

Annex I.

In Table 3 the charging experiments are marked in red, the discharging experiments in blue. During charging, the initial temperature of the storage was always set to 105 °C. For the discharging cases, experiments have been performed with two different initial temperatures of 138 °C and 150 °C.

In Section 3.1.1, the experiments C31, C32 and C33 as well as C11, C12 and C13 are used to show the effects of a mass flow rate variation on the storage power characteristics and the HTF liquid level in the tubes for two pressure stages during charging. The effects of a pressure variation for the charging process are presented in Section 3.1.2 using C11, C21 and C31 as examples.

C33, C31 and C11 demonstrate the effects of a pressure and a mass flow rate variation on the axial and radial temperature profiles in the storage in Section 3.2 as well as on the local heat transfer and liquid fraction in the storage in Section 3.3.

A short discussion of the mainly sensible discharging experiments on the effects of a mass flow rate variation for two different pressure stages on the storage power is presented in this article using the experiments D211, D212, D213 as well as D221, D222 and D223 in Section 3.1.3.

Table 3
Full measurement matrix for charging (red) and discharging (blue).

Phase Change Range (°C)	Initial Storage Temperature (°C)	Pressure HTF (bar)	Temperature HTF (°C)	Mass flow rate HTF (kg/h)	Experiment
118–137 (Charging)	105	3.0	134	1.44	C11
				2.16	C12
				2.88	C13
		4.5	148	1.44	C21
				2.16	C22
				2.88	C23
		6.7	163	1.44	C31
				2.16	C32
				2.88	C33
101–121 (Discharging)	138	1.4	109	1.26	D111
				2.78	D112
				4.30	D113
		1.7	115	1.26	D121
				2.68	D122
				4.10	D123
	150	1.4	109	1.26	D211
				2.78	D212
				4.30	D213
		1.7	115	1.26	D221
				2.68	D222
				4.20	D223

Annex II. (based on Dietz et al. [14])

Numerical Model

The numerical model approximates the transient conjugate processes in HTF and in the storage. It enables the simulation of operating modes where variable parts of the heat exchanger tubes are used for the phase change of the HTF and resolves the temperature field and the liquid fraction of the storage. Thus, the HTF-side operating condition and the formation of the phase change boundary in radial and axial directions can be correlated and linked to the corresponding thermal power characteristics.

Geometry described by the Numerical Model

The model is divided into an HTF part and a storage part, where the latter consists of the PCM and the fins. Fig. 16 shows the corresponding geometry. Regarding the considered dimensions, the HTF part is implemented one-dimensionally in the z-direction, and the PCM part two-

dimensionally in the z- and the r- direction. Both parts are coupled via an interface, which contains the wall properties. In the sketch r_{eff} is the effective storage radius.

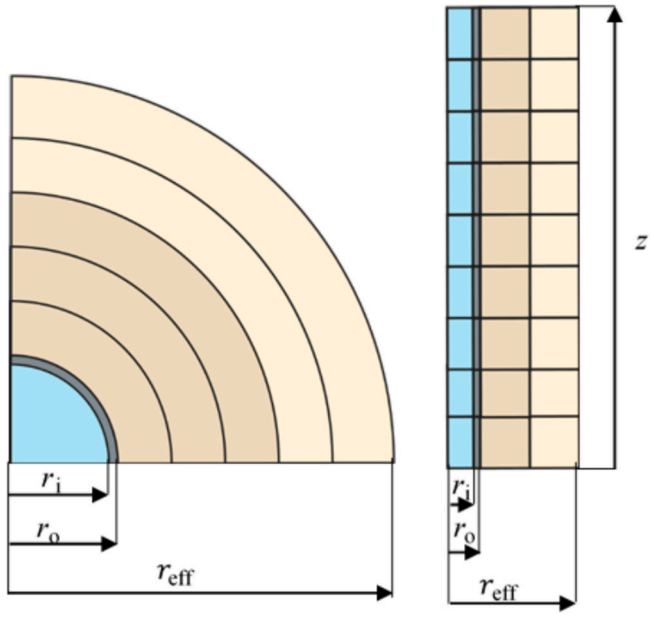

Fig. 16. Illustration of cross-sectional and longitudinal model geometry for the numerical model [17].

Assumptions for the numerical model

The model is tailored to simulate the heat transfer processes in large-scale LH-TES efficiently. This is achieved by the following simplifications of the physics [17].

1. Quasi-steady-state HTF flow: The processes in the HTF are much faster than the processes in the PCM which results in HTF equilibrium states for every PCM state.
2. 1D simulation of the HTF: No resolution of the HTF state in the radial direction.
3. Thermodynamic equilibrium in the HTF: It is assumed that the thermodynamic steam fraction is the actual steam fraction.
4. An effective fin model to represent the PCM/fin part of the storage is used, described in detail in [17].

Mathematical formulation of the numerical model

On the HTF-side, the first characteristic equation used is the equation of conservation of mass

$$\frac{\partial \mathrm{G_{HTF}}}{\partial \mathrm{z}} = 0, \tag{7}$$

with the mass flux G_{HTF} and the axial coordinate of the tube z. Secondly, the equation of conservation of momentum

$$\frac{\partial \mathrm{p_{HTF}}}{\partial \mathrm{z}} = \left(\frac{\partial \mathrm{p_{HTF}}}{\partial \mathrm{z}}\right)_{\mathrm{A}} + \left(\frac{\partial \mathrm{p_{HTF}}}{\partial \mathrm{z}}\right)_{\mathrm{G}} + \left(\frac{\partial \mathrm{p_{HTF}}}{\partial \mathrm{z}}\right)_{\mathrm{F}} \tag{8}$$

with the HTF pressure drops due to acceleration A, gravity G and friction F is implemented. The third characteristic equation is the equation of conservation of energy

$$\mathrm{G_{HTF}}\frac{\partial \mathrm{h_{HTF}}}{\partial \mathrm{z}} = \frac{\dot{q}_w \mathrm{A}_w}{\mathrm{V_{HTF}}} \tag{9}$$

with the specific enthalpy of the HTF h_{HTF}, the heat flux across the tube wall $\dot{q}_w$, the wall surface area A_w and the volume of the HTF V_{HTF}.

In the following, the constitutive equations of the model are introduced. The calculation of the volumetric steam fraction for boiling based on the heterogenous flow model is

$$\alpha_{\mathrm{HTF}} = \frac{\alpha_{\mathrm{HTF,H}}}{\mathrm{C_0} + \frac{v_{\mathrm{HTF,vap,j}}}{\mathrm{j_{HTF}}}} \tag{10}$$

with the heterogenous void fraction α_{HTF}, the homogenous void fraction $\alpha_{HTF,H}$, the distribution coefficient C_0, the drift velocity $v_{HTF,vap,j}$ and the volume flux j_{HTF}. For condensation,

$$\alpha_{\mathrm{HTF}} = \left(1 - \frac{2\delta_{\mathrm{HTF}}}{d_{\mathrm{tube}}}\right)^2 \tag{11}$$

is used with the condensation film thickness δ_{HTF} and the tube diameter d_{tube}. The frictional pressure drop is described by the Darcy-Weisbach equation for single-phase flow and by the Müller-Steinhagen and Heck correlation for two-phase flow.

A sum of the forced convection heat flux (FC), the boiling heat flux (B) and the condensation heat flux (C) describes the total transferrable heat flux

$$\dot{q} = \dot{q}_{FC} + \dot{q}_{B} + \dot{q}_{C} \tag{12}$$

and the forced convection Nusselt number is thereby calculated by the Dittus-Boelter equation

$$Nu_t = 0.023 Re^{0.8} Pr^{n} \tag{13}$$

with $n = 0.4$ for heating and $n = 0.3$ for cooling.

On the storage side, an effective fin model approximates a homogeneous storage material. Furthermore, the energy equation is transformed for the specific storage enthalpy using the enthalpy porosity method to

$$\rho_{stor} \frac{\partial h_{stor}}{\partial t} - \nabla(\lambda_{stor} \nabla T_{stor}) = \frac{S_{stor,b}}{V_{stor}} + S_{stor,pc} \tag{14}$$

with the density of the storage ρ_{stor}, the time t, the specific enthalpy h_{stor}, the thermal conductivity λ_{stor}, the temperature T_{stor} and the Volume V_{stor} of the storage, the boundary source term $S_{stor,b}$ and the source term for phase change $S_{stor,pc}$.

In the model, the liquid fraction f is defined by the storage temperaturerelated to the solidus temperature T_{sol} and the liquidus temperature T_{liq} of the PCM:

$$f = \begin{cases} 0, & T_{stor} \leq T_{PCM,sol} \\ 0...1, & T_{PCM,sol} < T_{stor} < T_{PCM,liq} \\ 1, & T_{stor} \geq T_{PCM,liq} \end{cases} \tag{15}$$

Further Details on the mathematical formulation of the model can be found in the original publication [17].

Data availability

Data will be made available on request.

References

[1] Intergovernmental Panel on Climate Change (IPCC) (Ed.), ed. Climate Change 2022 - Mitigation of Climate Change: Working Group III Contribution to the Sixth Assessment Report of the Intergovernmental Panel on Climate Change, Cambridge University Press, 2023.

[2] T. Fleiter, M. Rehfeldt, S. Hirzel, et al., CO2-neutrale Prozesswärmeerzeugung, 2023. Dessau-Roßlau.

[3] V. Jagadeeswara Reddy, M. Fairusham Ghazali, S. Kumarasamy, Innovations in phase change materials for diverse industrial applications: A comprehensive review, Results Chem. 8 (2024), https://doi.org/10.1016/j.rechem.2024.101552.

[4] W.-D. Steinmann, Thermal Energy Storage for Medium and High Temperatures, Springer Fachmedien Wiesbaden, Wiesbaden, 2022.

[5] Q. Li, C. Li, Z. Du, et al., A review of performance investigation and enhancement of shell and tube thermal energy storage device containing molten salt based phase change materials for medium and high temperature applications, Appl. Energy 255 (2019), https://doi.org/10.1016/j.apenergy.2019.113806.

[6] K. Theologou, L. Dietz, J. Tombrink, et al., Experimental characterization of a vertical shell-and-tube latent heat thermal energy storage with dual-tube finned tubes for evaporation at temperatures about 133 °C, J. Energy Storage 133 (2025), https://doi.org/10.1016/j.est.2025.117841.

[7] P. Garcia, M. Olcese, S. Rougé, Experimental and numerical investigation of a pilot scale latent heat thermal energy storage for CSP power plant, Energy Procedia 69 (2015) 842–849, https://doi.org/10.1016/j.egypro.2015.03.102.

[8] D. Laing, T. Bauer, D. Lehmann, et al., Development of a thermal energy storage system for parabolic trough power plants with direct steam generation, J. Sol. Energy Eng. 132 (2010), https://doi.org/10.1115/1.4001472.

[9] D. Laing, T. Bauer, N. Breidenbach, et al., Development of high temperature phase-change-material storages, Appl. Energy 109 (2013) 497–504, https://doi.org/10.1016/j.apenergy.2012.11.063.

[10] P. Garcia, G. Largiller, Performances and control aspects of steam storage systems with PCM: key learnings from a pilot-scale prototype, Appl. Energy 325 (2022), https://doi.org/10.1016/j.apenergy.2022.119817.

[11] P. Garcia, G. Largiller, G. Matringe, et al., Experimental results from a pilot scale latent heat thermal energy storage for DSG power plants – advanced operating strategies, AIP Conf. Proc. 2445 (2022) 160008, https://doi.org/10.1063/5.0085753.

[12] M. Johnson, M. Fiss, Superheated steam production from a large-scale latent heat storage system within a cogeneration plant, Comms. Eng. **2** (2023), https://doi.org/10.1038/s44172-023-00120-0.

[13] M. Johnson, J. Vogel, M. Hempel, et al., Design of high temperature thermal energy storage for high power levels, Sustain. Cities Soc. 35 (2017) 758–763, https://doi.org/10.1016/j.scs.2017.09.007.

[14] L. Dietz, I. Bürger, A. Gutierrez, Effect of steam flow parameters on the partial load behaviour of a PCM storage, J. Energy Storage 89 (2024), https://doi.org/10.1016/j.est.2024.111709.

[15] L. Dietz, T. Garbe, M. Fiss, et al., Experimental analysis of fluid flow and PCM storage in a single-tube steam generator, J. Energy Storage 116 (2025), https://doi.org/10.1016/j.est.2025.115754.

[16] D. Laing, M. Eck, M. Hempel, et al., Analysis of operation test results of a high temperature phase change storage for parabolic trough power plants with direct steam generation, in: ASME 6th Conference on Energy Sustainability, 2012. San Diego, USA.

[17] J. Vogel, M. Keller, M. Johnson, Numerical modeling of large-scale finned tube latent thermal energy storage systems, J. Energy Storage 29 (2020) 101389, https://doi.org/10.1016/j.est.2020.101389.